Finite element modelling of 3D orthogonal cutting experimental tests with the Coupled Eulerian-Lagrangian (CEL) formulation

F. Ducobu*, E. Rivière-Lorphèvre, E. Filippi

University of Mons (UMONS), Faculty of Engineering (FPMs), Machine Design and Production Engineering Lab, 20 Place du Parc, B-7000 Mons, Belgium

ABSTRACT

Most of the current finite element models of cutting concerns the 2D plane strain orthogonal cutting configuration, which, although of valuable interest to study the fundamental phenomena of the process, is still far from most practical cutting operations. The 3D models on the other side usually concern a 2D tool path with a cutting edge that is not straight any more. The step just after 2D orthogonal cutting is almost not addressed; it is the 3D orthogonal cutting. Based on an experimental reference of Ti6Al4V orthogonal cutting, this paper introduces a 3D finite element Coupled Eulerian-Lagrangian (CEL) model of orthogonal cutting that faithfully reproduces the experimental operation and is verified by comparison with it. Such a model and a comparison are not available in the current literature. A comparison is performed with a 2D orthogonal cutting model as well. The forces, the chip thickness and the lateral expansion of the chip were accurately modelled. The results showed that it is necessary to set the width of the workpiece large enough in order to get close to the plane strain assumption valid in the experimental configuration. A width of the workpiece equal to the uncut chip thickness constitutes a good compromise between the quality of the results and the number of nodes of the model. The Eulerian formalism of the workpiece mesh allowed to reduce its height and therefore the number of nodes without affecting the quality of the results. Moreover, this study showed that cubic elements should be adopted, as well as the addition of a range of elements that stays full of void and is parallel to the cutting plane at the boundary of the model to avoid influencing the results.

1. Introduction

Numerical modelling with the finite element method to study metal cutting was introduced at the beginning of the seventies [1]. Due to its high complexity and the large amount of phenomena it involves, the process is mostly studied in orthogonal cutting in order to mainly reduce the geometrical difficulties and the number of degrees of freedom of the models. The physical coupled phenomena (large strains, strain rates, at high temperatures and temperatures gradients, friction, and so on) must still however be considered and addressed, which leads to many publications. For more details, Arrazola et al. [2] present a review of metal machining modelling since 1998, while the review of Van Luttervelt et al. [3] concerns previous modelling works. Their great majority deals with 2D orthogonal cutting. While this configuration is really useful to understand the fundamental phenomena of cutting, it is far from the practical industrial applications and therefore industrial needs. As highlighted by Arrazola et al. [2], it is now time to move from 2D modelling to 3D in order to answer the demands of the industry.

3D finite element models of cutting do however already exist and

were reported in the literature. The geometrical configuration can be rather complex, depending on the process studied. Turning and drilling gather most of the publications up to now and some of them are presented in the following literature review. When the model concerns turning, the workpiece is nearly always simplified to a parallelepipedal block and the movement of the tool is linear, which is similar to a shaping operation. The curvature of the workpiece is ignored as its radius is assumed large enough for the short modelled cutting length. Guo and Liu [4] presented a 3D model of hardened AISI 52100 steel with a preformed chip as initial condition to help reaching the steady-state. The model of Aurich and Bil [5] was close to the previous one but it focused on the formation of segmented chip; no experimental validation was performed. Li and Shih [6] developed a 3D model for turning two grades of titanium with a focus on the chip curl. Arrazola and Özel [7] developed a 3D model of hard turning of AISI 4340 steel with an hybrid procedure involving a remeshing step followed by the transfer of the current results into a 3D Arbitray Lagrangian-Eulerian (ALE) model with Eulerian boundaries to model the steady-state of the process. The influence of the tool edge geometry was studied by Özel
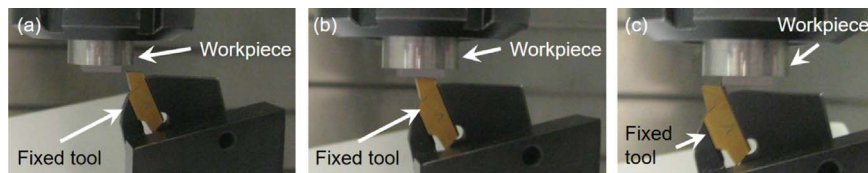

Fig. 1. Experimental test sequence (a) Beginning of the cut: the tool enters in the workpiece, (b) Cutting, (c) End of cut: the tool leaves the workpiece, adapted from Ducobu et al. [21].

[8] with a 3D model of turning AISI 4340 steel. Abaqus/Explicit and Deform 3D software were compared by Özel et al. [9] to machine Inconel 718. Özel and Ulutan [10] predicted the residual stresses with a 3D finite element model of turning Ti6Al4V and IN100 alloys. For drilling, Guo and Dornfeld [11] presented a 3D finite element model of drilling in 304L stainless steel to study burr formation. A more recent work of Abouridouane and al. [12] dealt with multi-phase material with a 3D two-phase drilling model of C45 steel. Modelling of milling introduces either the complex geometry of the tool, as Soo et al. [13] did with a 3D finite element model ball nose end-milling in Inconel 718, either the consecutive action of several teeth, as in the model of Pantalé et al. [1] in 42CrMo4 steel.

All the works listed so far have the complex geometry of a 3D operation and are consequently rather different of the simplified 2D orthogonal cutting configuration. A few works however deal with an intermediary configuration, which is the direct evolution of 2D orthogonal cutting: 3D orthogonal cutting and/or oblique cutting with a straight cutting edge. Fang and Zeng [14] presented a 3D finite element model of oblique cutting in ANSI 1045 steel; no experimental validation was provided. Pantalé et al. [15,16,1] developed a 3D ALE finite element model of orthogonal and oblique 42CrMo4 cutting. They highlighted a lateral expansion of the chip equal to 14% of the workpiece width. This lateral expansion is linked to a defect observed on the machined surface: the side flow, which is a material flow in the direction perpendicular to the chip flow [17]. The material sticks then to the machined surface and has a negative impact on its quality. It was studied experimentally by Kishawy and Elbestawi [17] in hard turning of AISI 4615 steel. They observed that the fraction of side flow on feed increases when feed decreases, that an increase in cutting speed increases the temperature which facilitates the side flow and that the side flow increases with the tool nose radius and the tool wear. Kishawy et al. [18] studied this side flow numerically in a 3D finite element model of multi pass hard turning of AISI 52100 steel. In the cutting conditions of the model, it was estimated between 2% and 10% of the feed (the feed was 0.1 mm/rev and the depth of cut was 0.25 mm) depending on the value of the tool nose radius. Attention was not paid to the side flow and/or the lateral expansion of the chip in the models other than that of Pantalé et al. [15,16,1] and Kishawy et al. [18], although it is a significant difference between 2D and 3D models.

Illoul and Lorong [19] applied another numerical method than the finite element to model 3D cutting. They used the Constrained Natural Element Method (CNEM) for 3D orthogonal and oblique cutting. Their objective was to show the capacity of the method to solve that kind of problems. No information was provided on the quality of the results and they were not compared to an experimental reference.

This overview of 3D numerical modelling of cutting showed that few models focused on the step just after 2D orthogonal cutting towards an industry-relevant 3D operation: 3D orthogonal cutting. The numerical results in this configuration were moreover almost not validated experimentally.

This paper performs this transition from 2D to 3D orthogonal cutting on the basis of a 2D Coupled Eulerian-Lagrangian (CEL) finite element model previously validated experimentally [20]. Lateral expansion of the chip is one of the phenomena to be addressed and that makes the difference with a 2D configuration. Although not yet of industrial interest, 3D orthogonal cutting is the preamble to oblique cutting, itself introducing industry-relevant complex 3D cutting with a

cutting edge and/or a tool path that is not straight any more. The modelled cutting operation is exactly the same as the experimental tests, which has not previously been seen in the literature. The 3D model will be introduced before being compared to the experimental results and to the results of the same model but in 2D. The 3D model will then be optimized in order to decrease the computing time and make it more useful in an industrial context. Then, the sensitivity of the results to the width of the workpiece will be studied. The 3D resulting model will finally be applied to two other uncut chip thicknesses values to show its predictive capacity and be compared to the experimental reference.

2. Experimental reference

The experimental setup introduced in [21] corresponds to a 3D orthogonal cutting configuration. It consists in removing the upper layer of the workpiece by a linear displacement of the workpiece (Fig. 1) towards the fixed tool. The configuration is similar to that of a planing operation. Such a setup provides strictly orthogonal cutting conditions in 3D that can be directly compared to the modelling as it corresponds to the same operation. The machined feature is a tenon of 1 mm width situated at the top of a cylindrical part (Fig. 2) fixed in the spindle (not rotating) of a Deckel-Maho DMU-80 T milling machine. The ratio between the uncut chip thickness, h, and the width of cut, b, is of at least 10 for the chosen cutting conditions of this work (width of cut is 1 mm and the largest uncut chip thickness value is 0.1 mm), which makes it suitable for the validation of 2D plane strain orthogonal cutting models.

The cutting conditions are summarized in Table 1. The machined material is the Ti6Al4V titanium alloy. Each cutting condition was repeated three times. The value of the cutting speed is limited to the maximal feed rate of the machine, 30 m/min. That value was adopted to stay in the recommended cutting speed range of the tool manufacturer [22]. The WC/Co tool is coated with TiN PVD. The forces were measured with a dynamometer Kistler 9257B. Their root mean square (RMS) values are given in Table 2. Chips were collected and embedded to be observed with an optical microscope after being polished. All of them were continuous. The average value (on 25 measurements for each uncut chip thickness) of their thickness values are provided in Table 2.

The lateral expansions of the chips, b', are provided in Table 3. The lateral expansion value is computed by the difference between the
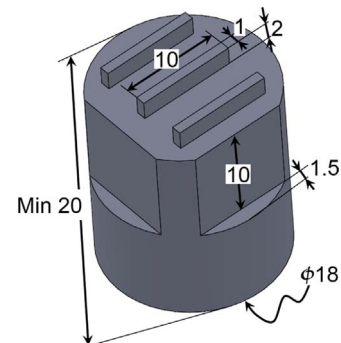

Fig. 2. Sample to be machined, dimensions in mm [21].

Table 1
Cutting conditions and tool geometry of the experimental reference [21].

Cutting speed, V_c (m/min)	30
Uncut chip thickness, h (μm)	40, 60, 100
Rake angle, γ (°)	15
Clearance angle, α (°)	2
Cutting edge radius, r (μm)	20
Width of the cutting edge (mm)	6

Table 2
Experimental cutting (CF) and feed (FF) forces average RMS values, chip thickness (h') average values [21].

h (μm)	RMS CF (N/mm)	RMS FF (N/mm)	h' (μm)
40	86 ± 2	40 ± 1	59 ± 5
60	113 ± 2	44 ± 1	80 ± 4
100	174 ± 2	50 ± 1	135 ± 6

Table 3
Experimental lateral expansion of the chips (b'), b'_x: ratio of b' to the length x (the uncut chip thickness, h, or the width of the workpiece, b). The experimental width of the workpiece, $b = 978 \pm 10.7$ μm.

h (μm)	b' (μm)	b'_b (% b)	b'_h (% h)
40	0.3 ± 6	0	1
60	12.6 ± 15	1	21
100	39.1 ± 16	4	39

measured width of the chip and the measured width of the tenon, b. For each uncut chip thickness, 10 measurements were performed. Two indicators, b'_b and b'_h, are introduced to quantify the magnitude of the lateral expansion of the chip: $b'_b = \frac{b'}{b}$ in % of the width of the workpiece b and $b'_h = \frac{b'}{h}$ in % of the uncut chip thickness h. They are introduced to show the magnitude of the lateral expansion by comparison to the width of the tenon, b, and the uncut chip thickness, h.

Standard deviation values on the experimental lateral expansion of the chips, b', are high: the variations of the width of the chips are significant compared to its lateral expansion. When $h=40$ μm and 60 μm, the standard deviation is larger than the average value, meaning that the width of the chips is smaller than the width of the tenon on some measured points. When comparing with the numerical works from the literature, the lateral expansion, in the experimental reference of this study, represents a smaller fraction of the width of the tenon ($b'_b = $ 0–4% versus ≈14% in the literature [16]) and a larger fraction of the uncut chip thickness ($b'_h = $ 1–39% versus 2–10% in the literature [18]). The evolution of b'_h is moreover the opposite of the trend reported in the literature [18]: it decreases when the uncut chip thickness decreases.

3. Finite element model

The 3D CEL finite element model introduced in this work is based on the 2D model experimentally validated in [20]. The tool is described by the Lagrangian formalism and the Ti6Al4V workpiece by the Eulerian one. This avoids the usual severe mesh distortions in a Lagrangian workpiece due to the large strains occurring during the cut. It is however necessary to mesh the volume where the chip will form contrary to the Lagrangian formulation, which increases the number of nodes of the model. Fig. 3 shows schematically the dimensions and the boundary conditions of the model. The cutting duration sets the workpiece length. It is chosen to have the lowest number of nodes but to form a chip long enough to be measured and to reach the steady-state for the cutting forces. The height of the area
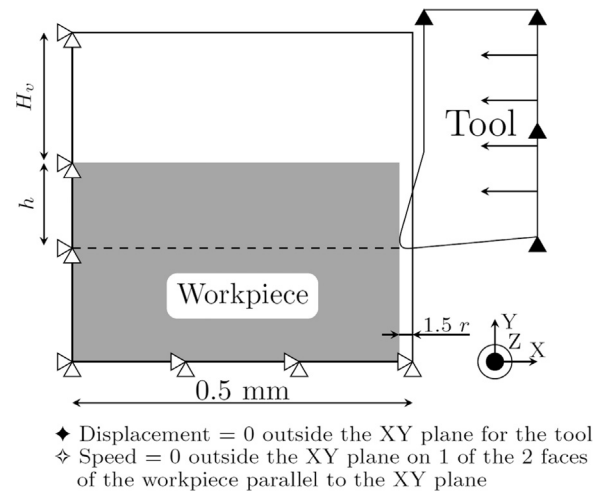

♦ Displacement = 0 outside the XY plane for the tool
♦ Speed = 0 outside the XY plane on 1 of the 2 faces of the workpiece parallel to the XY plane

Fig. 3. Schematic initial geometry and boundary conditions of the 3D model in a view perpendicular to the cutting plane XY (r: cutting edge radius, h: uncut chip thickness, H_v: height of the area initially filled with void).

above the workpiece in which the chip will develop, H_v, depends on the value of the uncut chip thickness in order to limit the number of nodes of the model. It is chosen to allow the chip to form entirely in the Eulerian mesh.

The workpiece is meshed with 8-node brick square elements of 5 μm×5 μm in the cutting plane XY. The tool is more coarsely meshed except near the edge radius where the elements length is 5 μm in the cutting plane. Fig. 4 presents the 3D initial conditions of the model, as well as the initial mesh with 13 elements in the width of the model for an uncut chip thickness of 60 μm. Half of the experimental workpiece width is modelled to take advantage of the symmetry of the configuration. One of the two external faces parallel to the cutting plane is considered as a plane of symmetry. No constraint on the degrees of freedom of the second face is applied in order to allow the free side of the chip to deform (and potentially expand) freely. The number of elements out of the cutting plane (in the Z direction, Fig. 4) is a parameter that will be further studied and discussed. It depends on the number of elements composing the workpiece and the elements added next to it (and initially filled with void) that will receive the material resulting of the lateral expansion of the chip and the side flow of the workpiece. Except for one particular case, the elements length in this
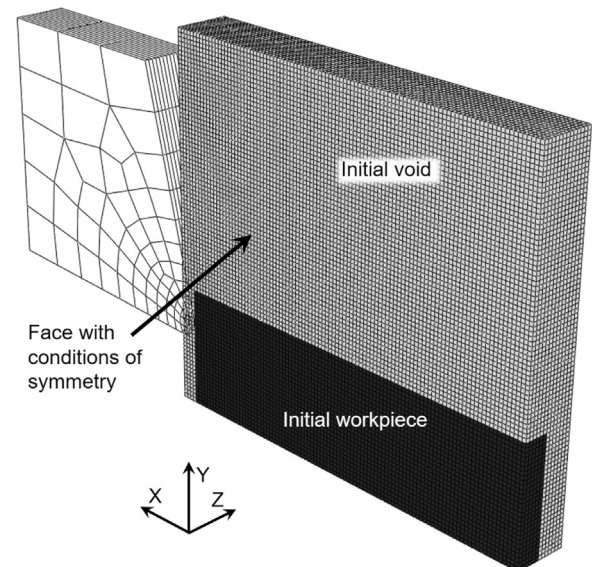

Fig. 4. In a 3D view: initial conditions and mesh of the 3D model for $h = $ 60 μm and a given width of the model.

Table 4
Materials properties of the numerical model [25–28].

JC constitutive model		
	A (MPa)	997.9
	B (MPa)	653.1
	C	0.0198
	m	0.7
	n	0.45
	$\dot{\varepsilon}_0$	1
	T_{room} (K)	298
	T_{melt} (K)	1878
Young's modulus, E (GPa)	Ti6Al4V	113.8
	Carbide	800
Density, ρ (kg/m^3)	Ti6Al4V	4430
	Carbide	15,000
Conductivity, k (W/mK)	Ti6Al4V	7.3
	Carbide	46
Expansion, α (K^{-1})	Ti6Al4V	8.6 e^{-6}
	Carbide	4.7 e^{-6}
Specific heat, c_p (J/KgK)	Ti6Al4V	580
	Carbide	203
Friction coefficient		0.2
Friction energy to heat (%)		100
Inelastic heat fraction		0.9
Heat partition to workpiece (%)		50

direction is the same, 5 μm, as in the cutting plane. The elements are thus cube-shaped. This is performed to avoid influencing the results with the shape of the elements.

The well-known, in metal cutting modelling, Johnson-Cook constitutive model [23] is adopted to describe the behaviour of the workpiece material, the Ti6Al4V titanium alloy:

$$\sigma = (A + B\,\varepsilon^{n})\left(1 + C\,\ln\frac{\dot{\varepsilon}}{\dot{\varepsilon}_0}\right)\left(1 - \left[\frac{T - T_{room}}{T_{melt} - T_{room}}\right]^{m}\right) \tag{1}$$

Parameters linked to the material properties are A, B, C, m and n. T_{melt} and T_{room} are, respectively, the melting and the room temperatures. $\dot{\varepsilon}_0$ is the reference strain rate. In accordance with the work of Ducobu et al. [24] on the choice of the Johnson-Cook set of parameters, the set of parameters adopted in this study comes from Seo et al. [25]; it is provided in Table 4. The tool material is tungsten carbide and it is described by a linear elastic model. In accordance with the experimental study of Rech et al. [26] performed in the same conditions of this work (same cutting speed, dry cutting, Ti6Al4V machined material, WC/Co cutting tool with TiN coating), friction at the tool – chip interface is modelled as Coulomb's friction. Concerning the thermal aspects, the faces of the model are adiabatic. The materials properties of the numerical model are given in Table 4. The cutting conditions are the same as for the experimental reference (Table 1).

4. Comparison of the 3D orthogonal cutting model with the experimental and numerical references

The 3D model is compared to the experimental reference and the 2D model in the same cutting conditions. The uncut chip thickness of 60 μm is adopted. The width of the 3D model (in the Z direction) is as small as possible to reduce the number of nodes: 1 element for the workpiece and 2 elements next to it (model called "1 narrow"); the total width of the model is thus 3 elements. The number of elements and nodes of both 2D and 3D models are given in Table 5, as well as the value of H_v. In all the models, the tool is as wide as the Eulerian mesh.

Both chips are plotted in a view perpendicular to the cutting plane in Fig. 5 (a) and (b); temperature contours are shown. In such views perpendicular to the cutting plane, temperature contours are selected to control if the high temperature area is in the second shear zone. This will contribute to check if the fundamental aspects of metal cutting are correctly modelled. Fig. 6 shows a 3D view of the chips. For the 3D model (Fig. 6 (b)), it is clearly seen that a fraction of the material expands so much in the Z direction that it goes outside of the mesh.

Table 5
Number of elements and nodes and value of H_v for the 2D model and the 3D models with 1 element of 5 μm in the width of the workpiece (narrow model: 3 elements in the width of the model, other models: 4 elements in the width of the model) for h=60 μm.

Model	Elements	Nodes	H_v (μm)
2D	8800	17,978	300
1 narrow	26,625	36,332	300
1	35,500	45,415	300
1, 50 μm	35,500	45,415	300

This means that the number of elements next to the initial workpiece is not large enough to allow the chip to expand freely outside of the cutting plane. This cannot be allowed and it is necessary to increase the width of the initial empty space modelled next to the workpiece.

One element is then added next to the workpiece, the workpiece width is still 1 element and the total width of the model is 4 elements (model called "1"). Figs. 5 (c) and 6 (c) present the chip for the model with 3 elements next to the workpiece. No material goes outside of the mesh any more although a lateral expansion of the chip is noticed. The maximal temperature is found in the secondary shear zone. This is in accordance with the expected chip formation process.

In Fig. 7 (a) and (b), it is however noticed that no material is found in the added elements and that almost no material is in the second layer of elements. The previous model with 2 elements next to the workpiece (model called "1 narrow") should therefore have given results in which no material flows outside of the mesh. From this observation, it is concluded that the material entering in the elements at the boundary of the Eulerian mesh is attracted outside of the mesh. To avoid this phenomenon, it is necessary to add a supplementary element that will stay full of void for the whole computation.

To increase the width of the workpiece for it to be closer to the experimental workpiece, the length of the elements is increased in the Z direction (perpendicular to the cutting plane) and it is checked if the shape of the elements alters the results. Figs. 5(d) and 6(d) show the only model in this study with an element length in the Z direction that is not 5 μm (model called "1, 50 μm"). The length adopted is 50 μm (so 10 times larger than the edges of the elements in the cutting plane) and 3 elements are added next to the workpiece. When visually comparing the chip morphology to that of the previous model in Fig. 6 (c) (the only difference between both models is thus the elements length outside of the cutting plane), it is clear that the shape of the elements influences the results. The lateral expansion of the chip, b', increases dramatically with the parallelepipedal elements and such a size is questionable.

From a general point of view, the lateral expansion of the chip mainly occurs in the area in contact with the tool. This is due to the fact that the material flows easily laterally when it is forced to deform by the tool as nothing constraints its displacement in this direction. To compare the order of magnitude of the lateral expansion of the chip with the experimental values, it is estimated in the numerical model from the views provided in Fig. 7. The experimental values were measured on the whole chip width and consequently with a lateral expansion on both sides of the chip. To compare the same experimental and numerical expansions, both full chips needs to be considered. Consequently, the numerical values are doubled to get the expansion on both sides of the chip as in the experiments.

Table 6 summarizes the results. For the model with 50 μm elements length, the value is large, as well as the difference with the experimental value. For the model with cubic elements, the lateral expansion is closer to the reference. The experiments showed that the lateral expansion is very small by comparison to the width of the chip but that it is significant by comparison to the uncut chip thickness. The ratio of the uncut chip thickness to the width of the tenon in the experiments is very large and the plane strain assumption can be adopted, as in the 2D model. In both 3D models, this ratio is smaller and it does not allow to adopt the plane strain assumption. As the
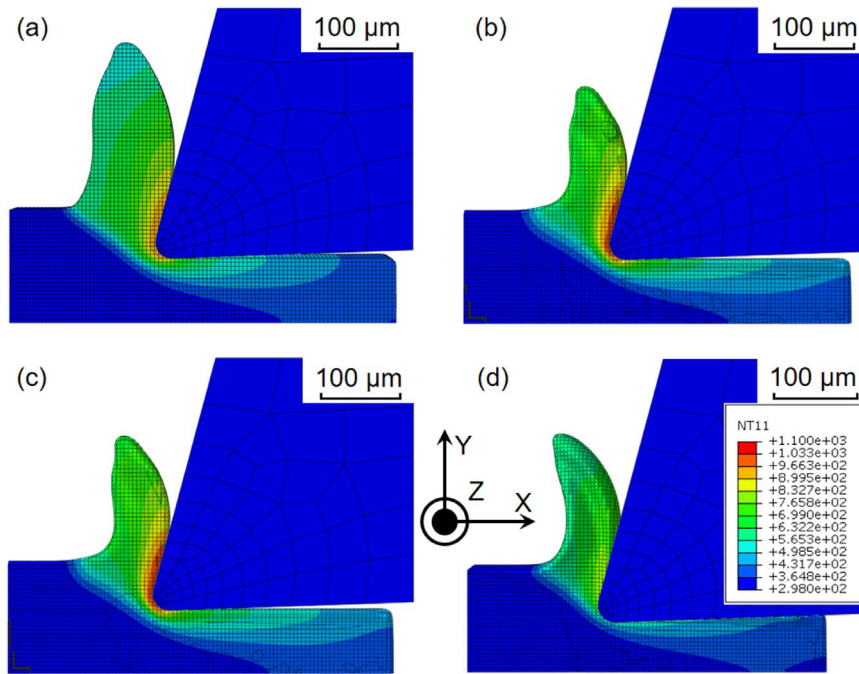
Fig. 5. Temperature contours (in K) of the numerical chips (a) 2D model, (b) 3D model with 1 element of 5 μm in the width of the workpiece (3 elements in the width of the model), (c) 3D model with 1 element of 5 μm in the width of the workpiece (4 elements in the width of the model) and (d) 3D model with 1 element of 50 μm in the width of the workpiece (4 elements in the width of the model) for h=60 μm after 600 μs of cutting in a view perpendicular to the cutting plane.

width of the tenon (i.e. the workpiece) is very small in the models, it was expected to have b'_b values larger than in the experiments, which is noted in Table 6. The values of b'_h can on the contrary be compared while keeping in mind that the plane strain conditions are not satisfied in the 3D models. Only a qualitative comparison is therefore wise. The value of b'_h for the model with elements of 5 μm in the width, very close to the experimental one, indicates more that the order of magnitude of the lateral expansion is similar, than the lateral expansion is accurately modelled. The very large value of b'_h when elements are 50 μm long in the width indicates that it is largely overestimated which was suspected from the chip morphology. The tendency of elongated elements to increase the lateral expansion is then confirmed. Cubic ("neutral") elements will therefore be adopted for the whole study and are recommended to avoid any influence of the elements shape on the results. Moreover when a predictive models is sought.

In the 3D numerical models, the measurement of the chip thickness is not trivial as its value is different depending on the distance of the plane in which it is measured with the plane of symmetry (Fig. 7). The adopted method consists in taking the mean of two thicknesses: the first one in the plane of symmetry (Figs. 8 (b) and (d)) and the second one in the plane of the lateral face of the workpiece (Figs. 8 (a) and (c)); 3 values are measured in each plane. For the 2D model, the thickness is, of course, the same in both planes. In the 3D model, the temperature

contours are different in the plane of symmetry and the lateral free plane, confirming the advantage of the 3D configuration to better represent the actual cutting process. The uncertainty on the plane in which the experimental value was measured needs to be pointed out. Indeed, as mentioned in the experimental reference section, the experimental chip thickness was measured on an embedded chip after polishing. It is therefore reasonable to take the mean of both numerical values as the experimental thickness was measured somewhere between the lateral face of the chip and its middle plane.

The thicknesses are provided in Table 7. The 2D model gives a thicker chip than the 3D models. This was expected as no lateral expansion is allowed in 2D. In 3D and in the experiments, a lateral expansion of the chip is allowed which leads to a thinner chip; the volume of the chip is conserved so a wider chip is thinner. When comparing with the experimental chip, the 3D values are closer than the 2D one, in accordance with the previous observation. The chip thickness values of both 3D chips are the same but their standard deviations are different. It is smaller for the cubic elements. This means that the thickness of the chip in both planes of measurement are closer than with the parallelepipedal elements. This was expected when looking at the lateral expansion of the chip with elongated elements in Figs. 6 and 7.

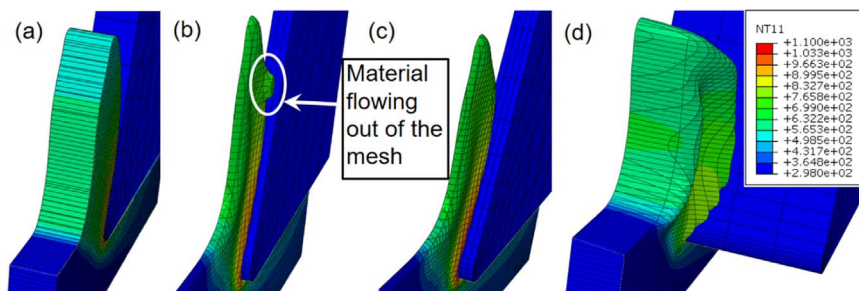All the chips are continuous (Fig. 5). Forces (cutting force, CF, in

Fig. 6. Temperature contours (in K) of the numerical chips (a) 2D model, (b) 3D model with 1 element of 5 μm in the width of the workpiece (3 elements in the width of the model), (c) 3D model with 1 element of 5 μm in the width of the workpiece (4 elements in the width of the model) and (d) 3D model with 1 element of 50 μm in the width of the workpiece (4 elements in the width of the model) for h=60 μm after 600 μs of cutting in a 3D view showing the lateral chip expansion.
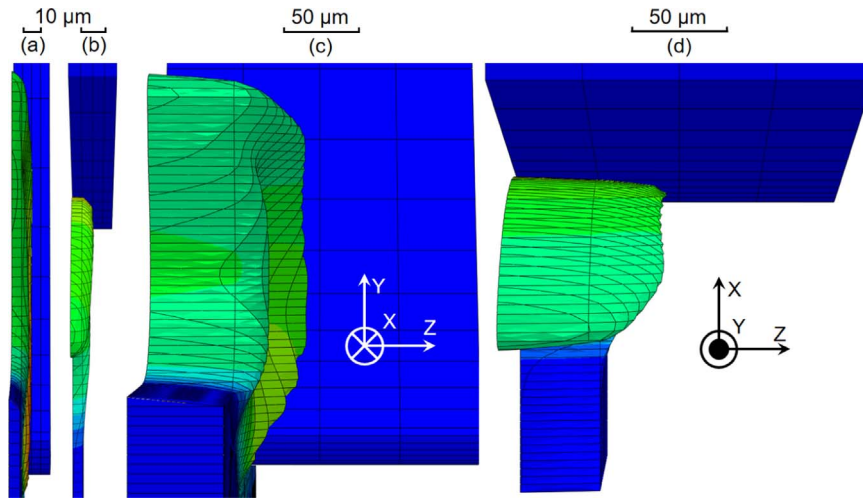
Fig. 7. Numerical chips (a) and (b) 3D model with 1 element of 5 μm in the width of the workpiece (4 elements in the width of the model), (c) and (d) 3D model with 1 element of 50 μm in the width of the workpiece (4 elements in the width of the model) for *h*=60 μm after 600 μs of cutting. (a) and (c) are seen from the end of the workpiece, (b) and (d) are seen from the top of the workpiece.

Table 6
Lateral expansion of the chip of the 3D models with 1 element in the width of the workpiece for *h* = 60 μm when comparing with the experimental reference, b'_x: ratio of b' to the length *x*.

Case Nber el.	b' (μm)	b'_b (% b)	b'_h (% h)
Exp.	12.6 ± 15	1	21
1	11.4 ± 3	114	19
1, 50 μm	84.9 ± 31	85	142

Table 7
RMS cutting forces and chip thickness summary of the 3D models with 1 element in the width of the workpiece for *h*=60 μm when comparing with the 2D model and the experimental reference, Δ_x: difference with the experimental values.

Case Nber el.	CF (N/mm)	Δ_{CF} (%)	FF (N/mm)	Δ_{FF} (%)	h' (μm)	$\Delta_{h'}$ (%)
Exp.	113 ± 2	–	44 ± 1	–	80 ± 4	–
2D	114	−1	34	22	99 ± 0	−24
1	123	−8	25	44	66 ± 2	18
1, 50 μm	109	4	30	33	66 ± 7	18

the X direction, feed force, FF, in the Y direction) with a nearly constant value when the steady-state of the cutting process is reached are therefore expected. Fig. 9 shows the forces evolutions obtained with the 3D model with 1 element of 5 μm. They are compared to the 2D

model and the RMS experimental values. Both 2D and 3D evolutions are very close and confirm that the steady-state is reached for the forces. The increase of the 3D forces is however slightly slower. This is
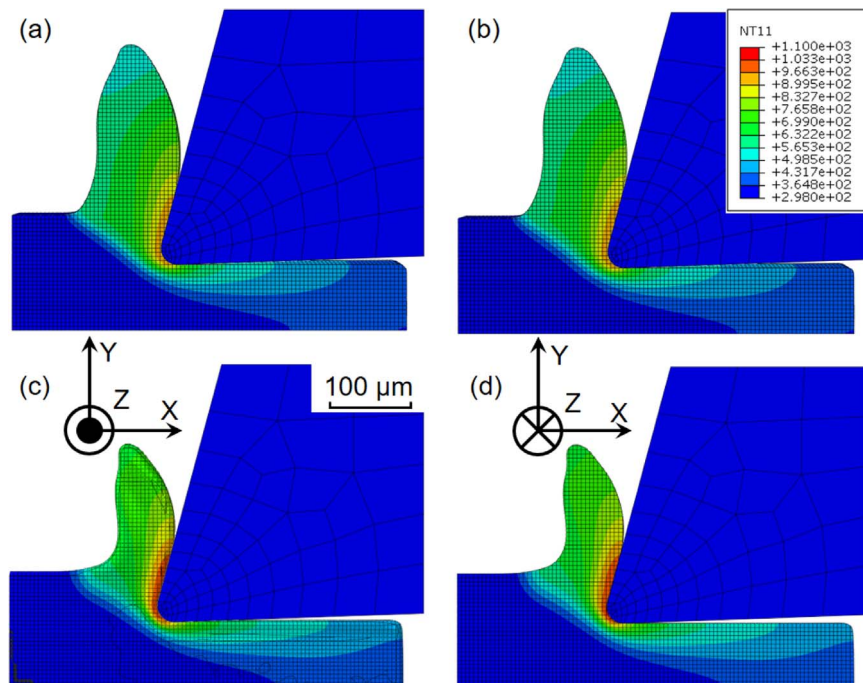

Fig. 8. Temperature contours (in K) of the numerical chips in 2 views perpendicular to the cutting plane (a) and (b) 2D model, (c) and (d) 3D model with 1 element of 5 μm in the width of the workpiece (4 elements in the width of the model) for *h*=60 μm after 600 μs of cutting. (a) and (c) are seen from the free plane side, (b) and (d) are seen from the plane of symmetry side.

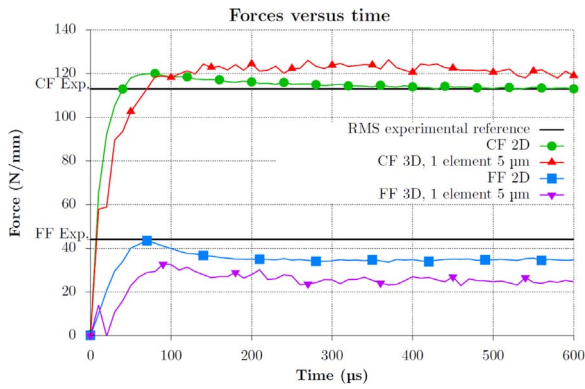**Fig. 9.** Typical forces evolutions for *h*=60 μm.

Table 8
RMS cutting forces and chip thickness summary of the 3D model with a low workpiece and 1 element of 5 μm in its width for *h*=60 μm when comparing with the references and the 3D model with the full workpiece, Δ_x: difference with the experimental values.

Case Nber el.	CF (N/mm)	Δ_{CF} (%)	FF (N/mm)	Δ_{FF} (%)	h' (μm)	$\Delta_{h'}$ (%)
Exp.	113 ± 2	–	44 ± 1	–	80 ± 4	–
2D	114	−1	34	22	99 ± 0	−24
1	123	−8	25	44	66 ± 2	18
1 low	122	−8	25	44	66 ± 2	18

explained by the lateral expansion of the chip which lengthens the time needed for the stable contact length between the tool and the chip to establish. Another difference with the 2D model is that the cutting force in 3D is slightly higher and the feed force in 3D is slightly lower, increasing the difference with the experimental reference. This is confirmed by the RMS values. The RMS cutting force in 3D is still accurately modelled while the feed force in 3D is more far from the reference. The change in the forces is explained by the change in the chip morphology. As it gets wider and thinner, the horizontal force needed to form it becomes larger and the vertical one becomes smaller.

In conclusion of this comparison, the model developed produces a chip with a 3D morphology and reproduces faithfully the experimental tests while taking advantage of the symmetry of the configuration. The lateral expansion of the chip is now modelled. The cutting force is accurately estimated and the difference with the experimental reference is larger for the feed force. The RMS forces values are closer to the experimental reference for the 2D model than the 3D one. The chip thickness is lower than the 2D model which is explained by the modelling of the lateral expansion in 3D. As the volume of the chip is the same, a wider chip ends in a smaller thickness. The 3D numerical thickness is closer to the experimental reference than the 2D one,

although it is underestimated contrary to the 2D model. As shown by the b'_b indicator, the lateral expansion takes however too much importance in the current 3D models. The width of the workpiece should therefore be increased in order to get closer to the plane strain assumption and the conditions of the experimental tests. This will dramatically increase the number of nodes of the model and it is proposed to reduce them in the current model before increasing its width.

5. Reduction of the number of Eulerian nodes

In order to decrease the number of nodes in the model, the height of the area initially filled with void, H_v, will now be reduced. The chips produced are continuous in the adopted cutting conditions. So, when the cutting regime is reached, the chip morphology and the forces hardly change with time. It would consequently make sense to only model the fraction of the chip close to the primary and secondary shear zones. A value of 60 μm =*h* for H_v is adopted (model called "1 low") and the results are compared to the model with the initial H_v value of 300 μm. This leads to the reduction of the number of nodes to 21,175 (45,415 with the full workpiece) and of elements to 16,300 (35,500 with the full workpiece). The reduction of the height of the workpiece will lead to a fraction of the material to flow out of the Eulerian mesh. This is classic in Eulerian meshes such as in computational fluid dynamics and no difference should arise from it.
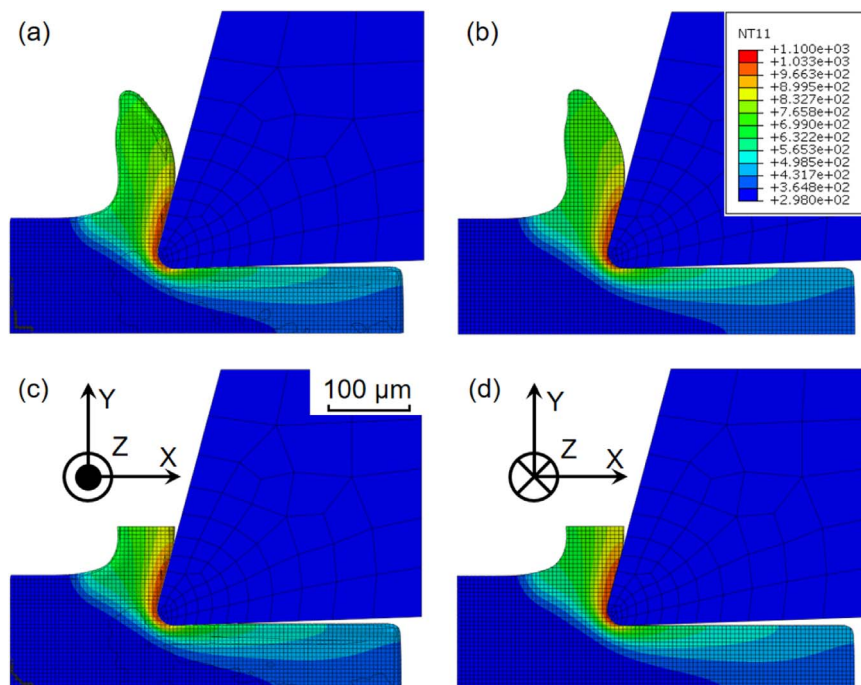

Fig. 10. Temperature contours (in K) of the numerical chips in 2 views perpendicular to the cutting plane (a) and (b) 3D model with 1 element of 5 μm in the width of the workpiece (4 elements in the width of the model), (c) and (d) low 3D model with 1 element of 5 μm in the width of the workpiece (4 elements in the width of the model) for *h*=60 μm after 600 μs of cutting. (a) and (c) are seen from the free plane side, (b) and (d) are seen from the plane of symmetry side.
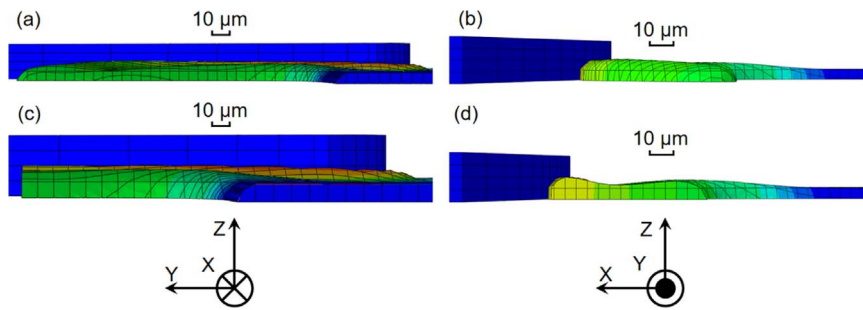
Fig. 11. Numerical chips (a) and (b) 3D model with 1 element of 5 μm in the width of the workpiece (4 elements in the width of the model), (c) and (d) low 3D model with 1 element of 5 μm in the width of the workpiece (4 elements in the width of the model) for h=60 μm after 600 μs of cutting. (a) and (c) are seen from the end of the workpiece, (b) and (d) are seen from the top of the workpiece.

Table 9
Lateral expansion of the chip of the 3D model with a low workpiece and 1 element of 5 μm in its width for h=60 μm when comparing with the experimental reference and the 3D model with the full workpiece, b'_x: ratio of b' to the length x.

Case Nber el.	b' (μm)	b'_b (% b)	b'_h (% h)
Exp.	12.6 ± 15	1	21
1	11.4 ± 3	114	19
1 low	10.8 ± 3	108	18

Table 10
Number of elements and nodes for the low 3D models with an increasing number of elements of 5 μm in the width of the workpiece for h=60 μm.

Model	Elements	Nodes	H_v
3 low	16,300	21,175	60
5 low	32,600	38,115	60
6 low	48,900	55,055	60
7 low	52,975	59,290	60
9 low	69,275	76,230	60
24 low	122,250	131,285	60

The chips morphologies of both models are qualitatively close in Fig. 10. In the cutting plane (Fig. 10 (d)), the results obtained with the low workpiece are similar to that of a 2D plane strain Arbitrary Lagrangian-Eulerian (ALE) model with Eulerian boundaries [27,29,26,30], but it has the advantage of being in a 3D configuration identical to the experiments and to keep the history of the material in the machined surface. As in the previous models, the maximal temperature is in the secondary shear zone as expected. The thickness values of both chips are equal as well as their standard deviation (Table 8) and their lateral expansion (Fig. 11 and Table 9). Similarly, both cutting and feed forces are equal.

This 3D model with a low workpiece can therefore be used to model the 3D orthogonal cutting operation of the experiments if the full chip geometry is not requested. It provides the same results as a model with a high workpiece but with the benefit of significantly reducing the number of nodes (by more than 50%).

6. Sensitivity of the results to the width of the workpiece

In order to come closer to the experimental workpiece, it is necessary to increase the width of the workpiece in the model. To limit the rise of the number of nodes, the low workpiece model configuration will be adopted. The number of elements in the width
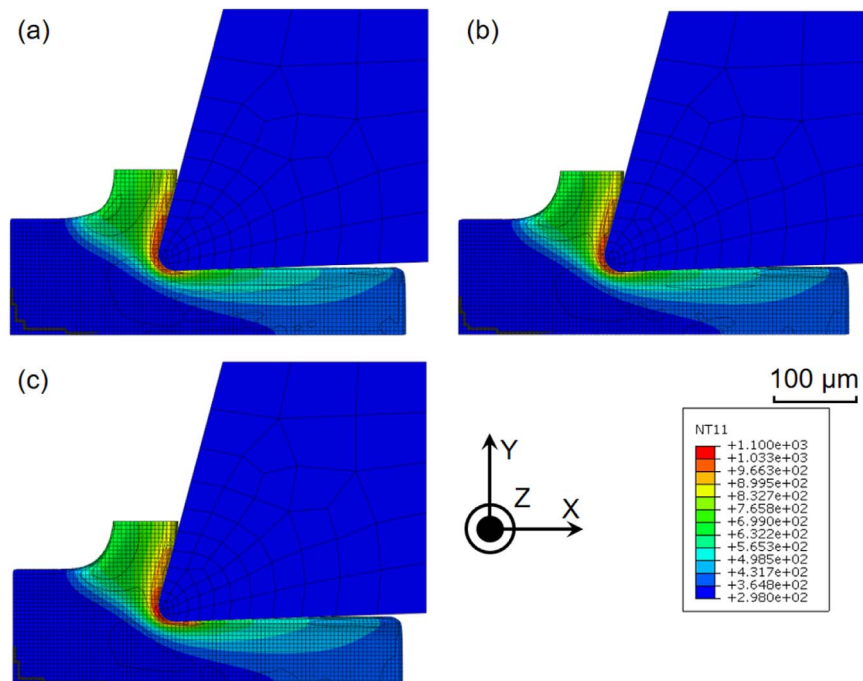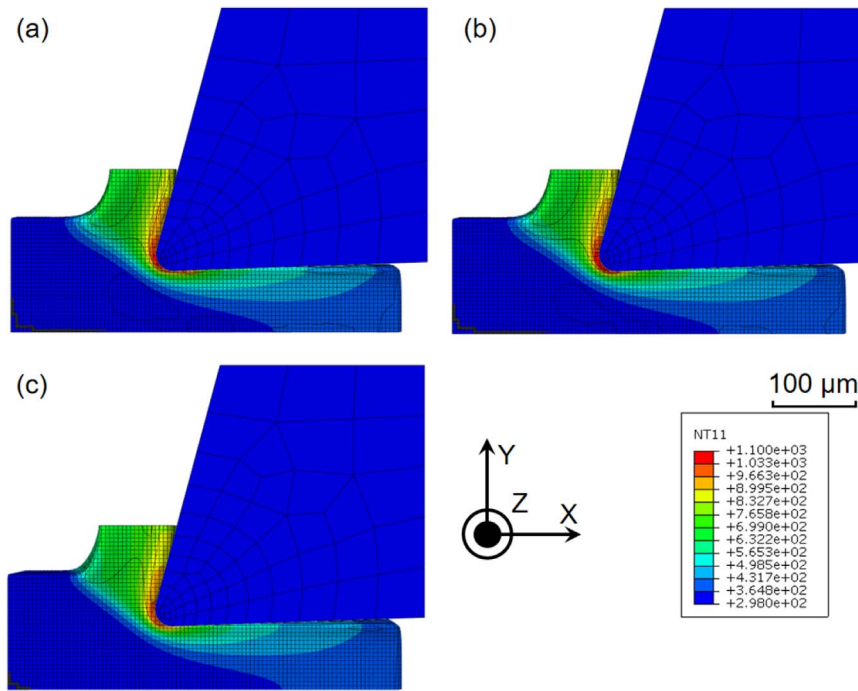

Fig. 12. Temperature contours (in K) of the numerical chips (a) low 3D model with 3 elements of 5 μm in the width of the workpiece, (b) low 3D model with 5 elements of 5 μm in the width of the workpiece and (c) low 3D model with 6 elements of 5 μm in the width of the workpiece for h=60 μm after 600 μs of cutting in a view perpendicular to the cutting plane.

Fig. 13. Temperature contours (in K) of the numerical chips (a) low 3D model with 7 elements of 5 μm in the width of the workpiece, (b) low 3D model with 9 elements of 5 μm in the width of the workpiece and (c) low 3D model with 24 elements of 5 μm in the width of the workpiece for h=60 μm after 600 μs of cutting in a view perpendicular to the cutting plane.

Table 11
RMS cutting forces and chip thickness summary of the low 3D models for an increasing number of elements of 5 μm in the width of the workpiece for h=60 μm when comparing with the 2D model and the experimental reference, Δ_x: difference with the experimental values.

Case Nber el.	CF (N/mm)	Δ_{CF} (%)	FF (N/mm)	Δ_{FF} (%)	h' (μm)	$\Delta_{h'}$ (%)
Exp.	113 ± 2	–	44 ± 1	–	80 ± 4	–
2D	114	−1	34	22	99 ± 0	−24
3 low	126	−11	28	36	74 ± 1	8
5 low	124	−10	29	33	77 ± 2	4
6 low	124	−9	30	31	78 ± 3	3
7 low	122	−8	31	30	79 ± 4	1
9 low	120	−6	32	28	83 ± 4	−4
24 low	114	−1	33	25	94 ± 9	−18

Table 12
Lateral expansion of the chip of the low 3D models for an increasing number of elements of 5 μm in the width of the workpiece for h=60 μm when comparing with the experimental reference, b'_x: ratio of b' to the length x.

Case Nber el.	b' (μm)	b'_b (% b)	b'_h (% h)
Exp.	12.6 ± 15	1	21
3 low	32.4 ± 10	108	54
5 low	42.3 ± 17	85	70
6 low	38.3 ± 16	64	64
7 low	41.2 ± 14	59	69
9 low	37.1 ± 20	41	62
24 low	16.3 ± 39	7	27

of the workpiece goes from 3 to 24 (i.e. a modelled width from 15 μm to 120 μm). Table 10 presents the number of elements and nodes of the six models considered. It is interesting to highlight the benefit of using a low workpiece for the number of nodes in the model. For example, when 6 elements are in the width of the workpiece, the number of nodes of the model (55,055) is only slightly higher than the model with the full height of the workpiece (45,415) but with only 1 element in the width.

Figs. 12 and 13 present the 6 chips obtained after 600 μs of simulation. They seem rather close and the high temperature area is still the secondary shear zone. It seems however that the rigidity of the chip increases with the number of elements in the width. When comparing the two extreme cases in Fig. 12 (a) and Fig. 13 (c), it is indeed noticed that the contact length is longer for the wider chip of Fig. 13 (c). The thickness of the chip seems to increase as well.

The measured values of the chip thickness (Table 11) confirm the visual observations. It increases with the width of the workpiece. As the thickness was lower than the experimental reference for the workpiece with 1 element in its width, it comes closer to the reference but it then oversteps it for the two wider workpieces. The larger value is still however lower than that of the 2D model. The forces values are influenced by the chip morphology (as in the previous section), showing that the phenomena are correctly captured by the model. When the width increases, the cutting force decreases and the feed force increases towards the reference values. For the wider workpiece, the cutting force is nearly equal to the reference value, while the feed force is still underestimated by 25%, which is similar to the results of the 2D model. As the 3D model comes closer to the plane strain conditions, its results come closer to that of the 2D model.

Concerning the lateral expansion of the chip, the values shown in Table 12 exhibit globally a decrease towards the experimental values. The difference with the reference for the wider chip is still noticeable but the evolution is clear. The standard deviations are large. Except for the wider workpiece, their values are however close to that of the experiments. Figs. 14 and 15 and particularly the (b), (d) and (f) cases clearly show why the standard deviation values of h' and b' increase with the width of the workpiece when looking at the chip morphology. It is clearly seen that the thickness of the chip is not constant through its width: it is thicker in the plane of symmetry and decreases towards the lateral free plane. This confirms that it is necessary to measure the thickness in both planes as the experimental measurement plane position is unknown. For the lateral expansion, it is larger for the zone of the chip in contact with the tool as previously observed.

In conclusion, the global tendencies are clear for the results when the width of the workpiece increases: except for the chip thickness, they
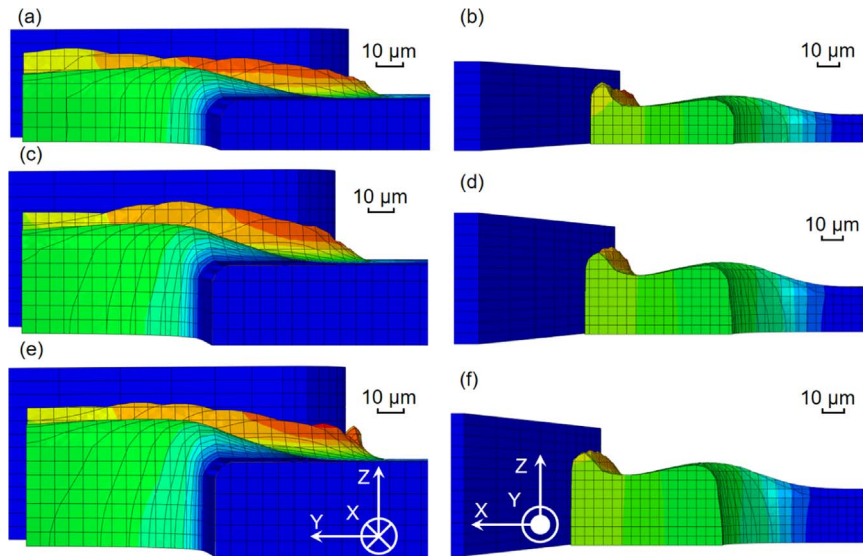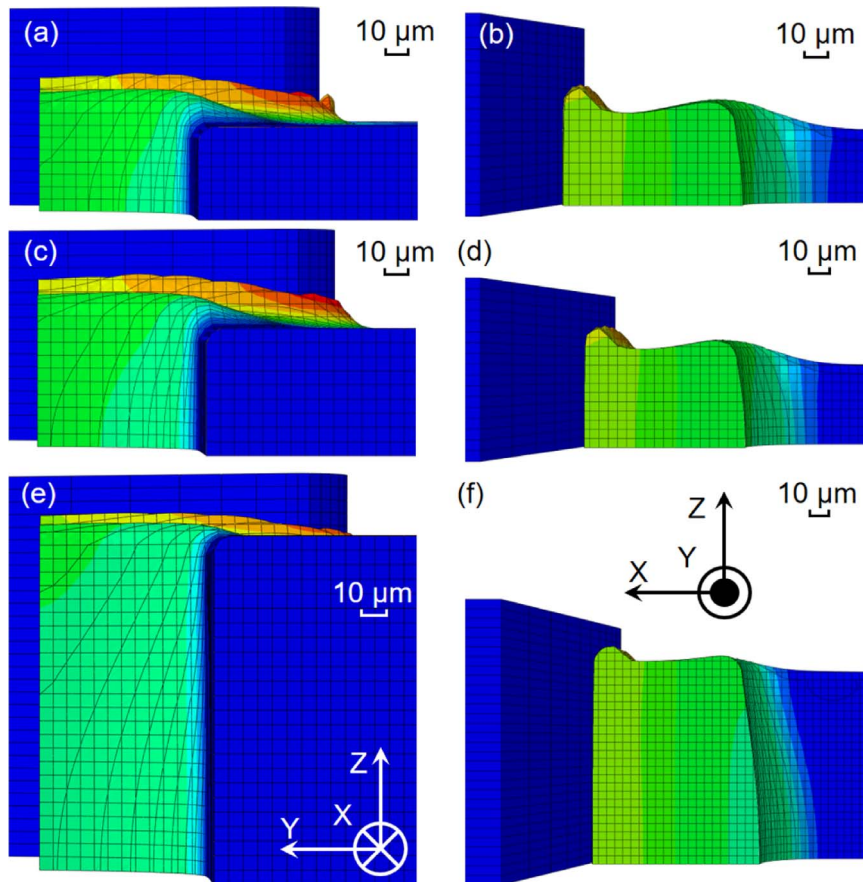
Fig. 14. Numerical chips (a) and (b) low 3D model with 3 elements of 5 μm in the width of the workpiece, (c) and (d) low 3D model with 5 elements of 5 μm in the width of the workpiece, (e) and (f) low 3D model with 6 elements of 5 μm in the width of the workpiece for $h=60$ μm after 600 μs of cutting. (a), (c) and (e) are seen from the end of the workpiece, (b), (d) and (f) are seen from the top of the workpiece.

Fig. 15. Numerical chips (a) and (b) low 3D model with 7 elements of 5 μm in the width of the workpiece, (c) and (d) low 3D model with 9 elements of 5 μm in the width of the workpiece, (e) and (f) low 3D model with 24 elements of 5 μm in the width of the workpiece for $h=60$ μm after 600 μs of cutting. (a), (c) and (e) are seen from the end of the workpiece, (b), (d) and (f) are seen from the top of the workpiece.

all get closer to the experimental and numerical references. Increasing the width of the workpiece leads to a model closer to the plane strain assumption valid in the experiments and the 2D model. The evolution of the results for the 3D models makes therefore sense. The next step would consequently be to continue the increase of the width of the workpiece to reach that of the experimental workpiece. The number of nodes it would require (roughly estimated at 470,000) is too large and it is currently not realistic to develop such a model.

In order to obtain results with a model useful in an industrial context, a compromise between the quality of the results and the number of elements is required. The model with 6 elements in the width of the workpiece is a good candidate. The forces are rather well
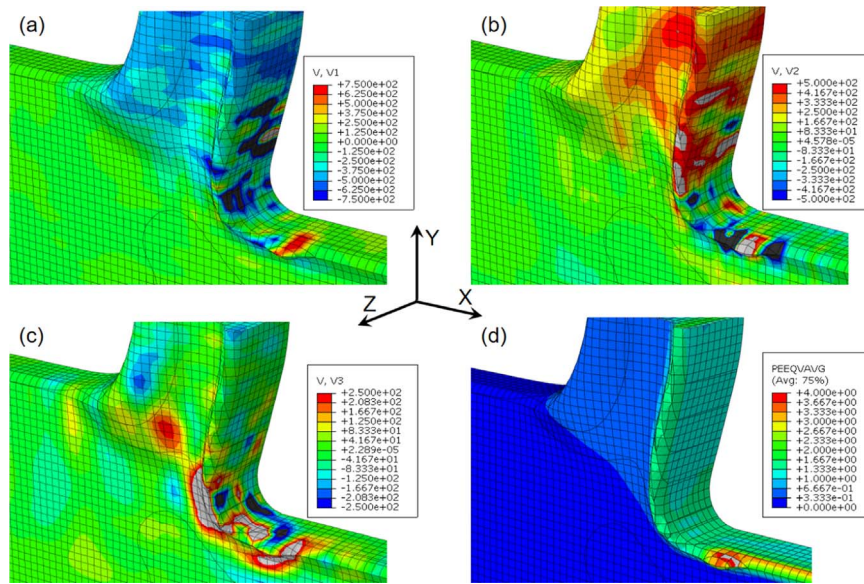
Fig. 16. Velocity contours (in mm/s) (a) direction −X, (b) direction Y, (c) direction Z and (d) equivalent plastic strains.
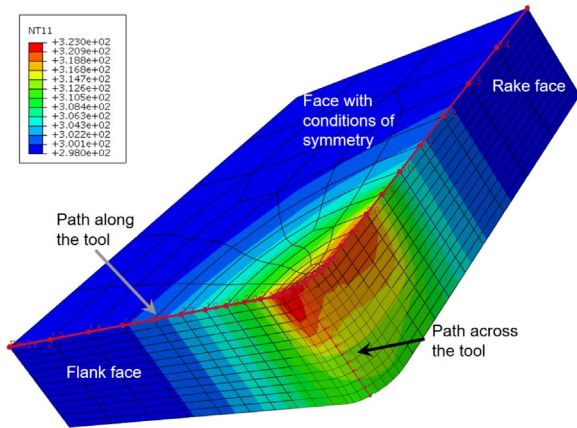

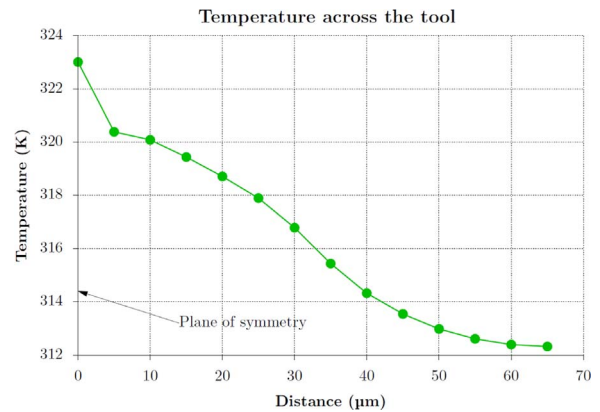**Fig. 17.** Temperature contours (in K) of the tool after 600 μs of cutting.

Fig. 19. Evolution of the temperature across the tool after 600 μs of cutting.

Table 13
Number of elements and nodes and value of H_v for the 2D and 3D models for h=40 μm and h=100 μm.

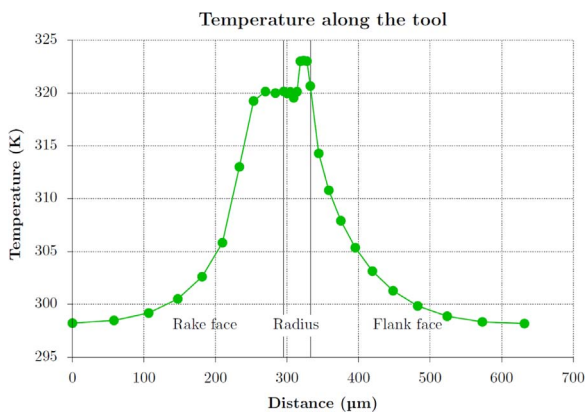| Model	Elements	Nodes	H_v
40 μm, 2D	6,875	14,126	220
40 μm, 3D	32,750	37,697	40
100 μm, 2D	10,075	20,590	320
100 μm, 3D	97,500	105,903	100

Fig. 18. Evolution of the temperature along the tool in the plane of symmetry after 600 μs of cutting.

estimated and the chip morphology, although not the closest to the reference, is globally well reproduced. Moreover, the computed workpiece has a width equal to half of the uncut chip thickness. It then provides information on a chip with a width equal to the uncut chip thickness value thanks to the symmetry of the configuration. This provides an objective criterion to select the width of the workpiece for the 3D model.

7. Focus on some aspects of the chip formation

The model with 6 elements in the width of the workpiece for an uncut chip thickness of 60 μm is studied more deeply in this section with a focus on chip morphology and the lateral expansion of the chip. Velocity contours are plotted in Figs. 16 (a)–(c). They contribute to understand the chip shape and its lateral expansion. For the nodes velocity in the cutting speed direction (Fig. 16 (a), direction −X), all the nodes of the chip go in the same direction as the tool as it pushes them. In the vertical direction (Fig. 16 (b), direction Y), all the nodes of the chip have a movement in the upper direction. This means that the chip grows. In the third direction, outside of the cutting plane (Fig. 16 (c), direction Z), the nodes velocity is positive near the cutting radius. This means that these nodes are pushed laterally outside of the cutting plane, confirming the lateral expansion of the chip. Fig. 16 (d) shows
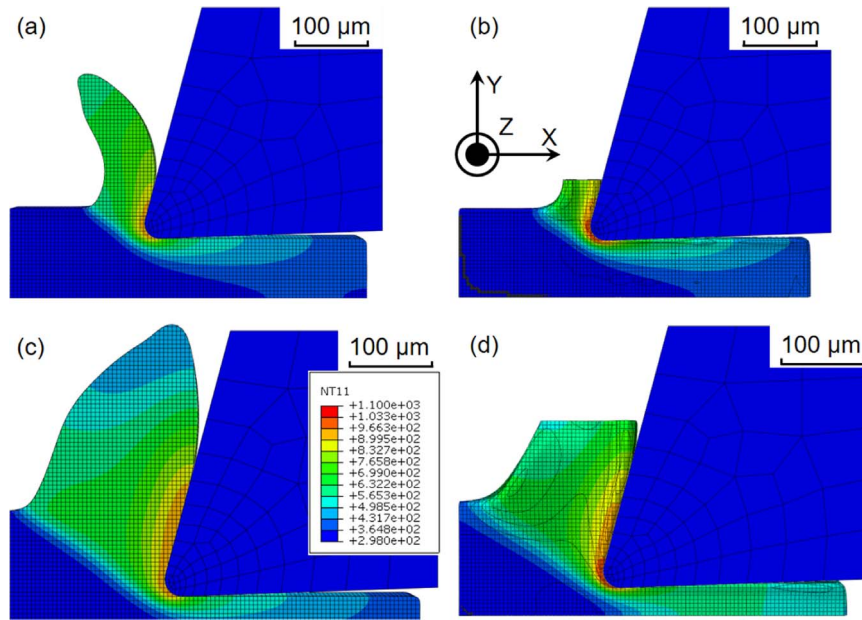
Fig. 20. Temperature contours (in K) of the numerical chips (a) 2D model for h=40 μm, (b) low 3D model with 4 element of 5 μm in the width of the workpiece for h=40 μm, (c) 2D model for h=100 μm and (d) low 3D model with 10 element of 5 μm in the width of the workpiece for h=100 μm after 600 μs of cutting in a view perpendicular to the cutting plane.

Table 14
RMS cutting forces and chip thickness summary of the 3D models for h=40 μm and h=100 μm when comparing with the 2D models and the experimental references, Δ_x: difference with the experimental values.

Case	CF (N/mm)	Δ_{CF} (%)	FF (N/mm)	Δ_{FF} (%)	h' (μm)	$\Delta_{h'}$ (%)
40, exp.	86 ± 2	–	40 ± 1	–	59 ± 5	–
40, 2D	84	2	36	9	67 ± 1	−14
40, 3D	93	−8	33	19	50 ± 2	15
100, exp.	174 ± 2	–	50 ± 1	–	135 ± 6	–
100, 2D	171	2	31	38	165 ± 1	−22
100, 3D	184	−6	27	47	128 ± 7	5

Table 15
Lateral expansion of the chip of the 3D models for h=40 μm and h=100 μm when comparing with the experimental references, b'_x: ratio of b' to the length x.

Case Nber el.	b' (μm)	b'_b (% b)	b'_h (% h)
40 μm exp.	0.3 ± 6	0	1
40 μm 3D	27.2 ± 11	68	45
100 μm exp.	39.1 ± 16	4	39
100 μm 3D	66.5 ± 17	66	66

the equivalent plastic strains. They are larger for the material near the cutting radius and the rake face. The plastic strains are even more large for the material that has been laterally expanded. This has an influence on the quality of the machined surface: a fraction of this highly deformed material is on the exterior side of the workpiece.

Fig. 17 presents the temperature contours of the tool. The CEL formulation in Abaqus v6.14 does not allow to take into account the thermal transfers between the Eulerian (the workpiece) and the Lagrangian (the tool) parts. Consequently, the increase of temperature at the interface between both parts is due to the friction energy converted into heat The temperature on the tool is lower than what could be expected and the time to reach its temperature steady state is longer. The results presented on the tool temperatures has therefore to be analysed with that information in mind and should be considered as a qualitative tendency and not quantitative temperatures values. The maximal temperature area is in the secondary shear zone and in the

cutting radius. Maximal temperatures are measured in the plane of symmetry of the model, as expected. This is confirmed by the temperature evolution along (Fig. 18) and across (Fig. 19) the tool. The temperature increases when getting closer to the edge radius and closer to the plane of symmetry.

8. Validation of the approach at the two other uncut chip thicknesses of the experiments

The 3D model of orthogonal cutting developed in this work has considered only one cutting condition so far. For it to be useful in an industrial context and to be predictive, it has to be able to handle other cutting conditions. This section is intended to assure that results in other cutting conditions than that adopted to develop the model are still in accordance with the experimental reference.

The model with 6 elements in the width of the workpiece has been selected to model the orthogonal cutting with an uncut chip thickness of 60 μm. This corresponds to a model with a workpiece width equal to half of the uncut chip thickness (30 μm). The 3D modelling of orthogonal cutting will now be extended to the two other uncut chip thicknesses of the experimental reference, h=40 μm and h=100 μm. The 3D model configuration with the low workpiece is kept to reduce the number of nodes. The same method as for h=60 μm is adopted and the height of the area initially filled with void, H_v, is set to the uncut chip thickness value. The number of nodes and elements are compared to that of the corresponding 2D models in Table 13.

Fig. 20 compares the chips morphologies between the 2D and the 3D models for the two uncut chip thicknesses. In all the cases, the maximal temperatures area is in the secondary shear zone, showing that the chip formation is correctly modelled. As expected from the results at h=60 μm and Fig. 20, the chip thicknesses values of the 3D models given in Table 14 are smaller than for the 2D models. They are closer to the experimental reference for the 3D models than the 2D ones. The difference with the reference is similar to that at h=60 μm for h=100 μm, while it is larger at h=40 μm.

Concerning the cutting forces RMS values (Table 14), although they are close to the reference, the difference is larger than for the 2D models as previously observed. The same is noted for the feed forces RMS values for which the difference with the experimental reference is larger. These results are in accordance with that at h=60 μm.
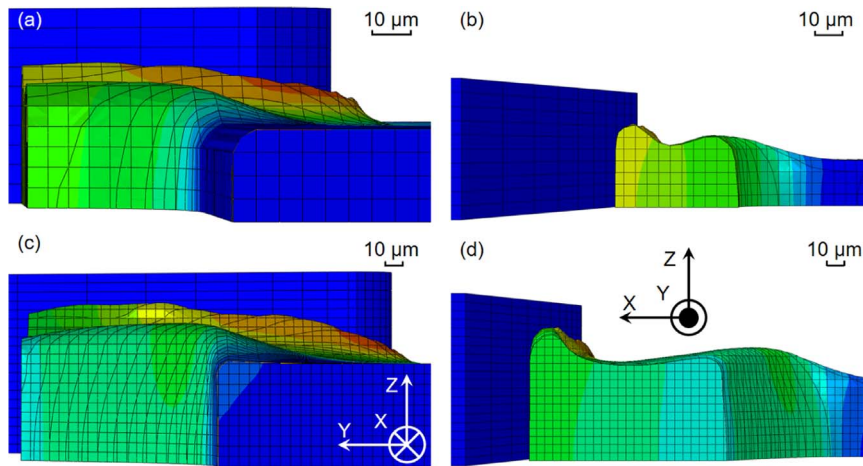
Fig. 21. Numerical chips (a) and (b) low 3D model with 4 element of 5 μm in the width of the workpiece for *h*=40 μm, (c) and (d) low 3D model with 10 element of 5 μm in the width of the workpiece for *h*=100 μm after 600 μs of cutting. (a) and (c) are seen from the end of the workpiece, (b) and (d) are seen from the top of the workpiece.

Table 16
Computation time variations for 10 μs of simulation.

Model	Time variation (%)
2D	−73
1 narrow	−55
1	−44
1, 50 μm	−33
1 low	−68
3 low	−38
5 low	−7
6 low	0
7 low	20
9 low	32
24 low	153
40 μm, 2D	−78
40 μm, 3D	−36
100 μm, 2D	−72
100 μm, 3D	65

The lateral chip expansion values (Table 15) are estimated by the same method as at *h*=60 μm (Fig. 21). The numerical values are again larger than for the experiments. This was expected due to the same configuration, still not entirely satisfying the plane strain assumption valid in the experiments. An increasing tendency with the uncut chip thickness was experimentally observed for b'_h. It is as well for the modelling but the increase is less significant. All the indicators are therefore globally accurately captured for the 3D models by comparison with the experimental reference and the developed 3D model can be validated to model the 3D orthogonal cutting of Ti6Al4V.

9. Computation time

The Abaqus simulations are run on a supercomputer, Dragon1. This contributes to reduce the computation time but it becomes more difficult to compare the computation times between two simulations. Indeed, for the same simulation, the computation time varies greatly (of more than ± 20%) depending on the load of the supercomputer. As this load cannot be controlled, it is not possible to obtain reliable and reproducible computation times. To give an order of magnitude, for the model with 6 elements in the width of the workpiece for an uncut chip thickness of 60 μm, around 13 h are needed to compute 600 μs with 4 Intel SandyBridge 2.60 GHz processors.

Table 16 presents the variation of the computation time for the different models of this study. These variations are obtained by taking the model with 6 elements in the width of the workpiece for an uncut chip thickness of 60 μm as a reference. To avoid the influence of the load of the supercomputer, 10 μs of simulation are computed on an Intel i7-5700 HQ 3.48 GHz processor for each model. The very small variation of the stable time increment for a CEL model [20] guarantee the representativeness of this short simulation time.

The computation times evolve as expected: the computation increases with the width of the workpiece (for a same uncut chip thickness and a same workpiece height: models "1 low" to "24 low") and with the height of the workpiece (for a varying uncut chip thickness: models "6 low", "40, 3D" and "100, 3D" or at the same uncut chip thickness but with a low or a complete workpiece: models "1" and "1 low'). The aspect ratio of the elements influences the computation time: cube-shaped elements lead to a lower computation time than parallelepipedal elements for the same number of elements and nodes (models "1'" and "1, 50 μm"). Finally, it is significantly lower for 2D models as their number of nodes is smaller.

10. Conclusions

A 3D model of orthogonal cutting has been introduced. It faithfully reproduces the experimental tests, with a thinner workpiece. The true numerical reproduction of a 3D orthogonal cutting operation with its experimental validation has not been carried out previously in the literature. It is a first step towards the modelling of an industry-relevant operation. This work allowed to model more accurately orthogonal cutting experiments by including phenomena occurring outside of the cutting plane, such as the lateral expansion of the chip. The main highlights of the study are:

- It is recommended to adopt cube-shaped elements for the Eulerian mesh to avoid influencing the results. The machined material was indeed attracted in the elongated direction of the elements. It is also recommended to leave a row of elements in which the material will not flow at the boundary of the Eulerian mesh to avoid an attraction effect of the material out of the mesh.
- The forces were accurately modelled and particularly the cutting force, which shows a difference with the experimental values of less than 10%. An increase of the width of the workpiece brought the forces values closer to the reference. This is due to the uncut chip thickness to chip width ratio, $\frac{h}{b}$, that gets closer to the plane strain assumption valid in the experiments and the 2D model.
- The lateral chip expansion was modelled and is the main difference by comparison to a 2D model. Nodes velocity and equivalent plastic strains contributed to explain the chip morphology and its lateral expansion. This lateral expansion of the chip however took too much importance by comparison to the width of the workpiece and the uncut chip thickness but its value decreased with a wider workpiece,

which is closer to the plane strain assumption.

- The evolutions of the model results with the width of the workpiece showed that it is necessary to increase it to reduce the difference with the experimental reference. Increasing the width of the workpiece however increased significantly the computation time due to the rise of the number of nodes of the model.

- To keep a reasonable number of nodes in the 3D model, it was proposed to adopt a workpiece width equal to half of the uncut chip thickness. This gives results for a workpiece of a width equal to the uncut chip thickness as only half of it is modelled by taking advantage of the symmetry of the configuration. With an height of the domain in which the chip can form equal to the uncut chip thickness value, this ended in a model exploitable in an industrial context and providing results with a satisfactory accuracy in 3D orthogonal cutting.

Acknowledgements

References

[1] O. Pantalé, J.-L. Bacaria, O. Dalverny, R. Rakotomalala, S. Caperaa, 2D and 3D numerical models of metal cutting with damage effects, Comput. Methods Appl. Mech. Eng. 193 (2004) 4383–4399.

[2] P. Arrazola, T. Özel, D. Umbrello, M. Davies, I. Jawahir, Recent advances in modelling of metal machining processes, CIRP Ann. - Manuf. Technol. 62 (2013) 695–718.

[3] C.V. Luttervelt, T. Childs, I. Jawahir, F. Klocke, P. Venuvinod, The State-of-the-Art of modelling in machining processes, CIRP Ann. - Manuf. Technol. 47 (1998) 587–626.

[4] Y. Guo, C. Liu, 3D FEA modeling of hard turning, J. Manuf. Sci. Eng. 124 (2002) 189–199.

[5] J. Aurich, H. Bil, 3D finite element modelling of segmented chip formation, Ann. CIRP 55 (2006) 47–50.

[6] R. Li, A.J. Shih, Finite element modeling of 3D turning of titanium, Int. J. Adv. Manuf. Technol. 50 (2005) 825–833.

[7] P. Arrazola, T. Özel, Numerical modelling of 3d hard turning using arbitrary lagrangian eulerian finite element method, Int. J. Mach. Mach. Mater. 3 (2008) 238–249.

[8] T. Özel, Computational modelling of 3D turning: influence of edge micro-geometry on forces, stresses, friction and tool wear in PcBN tooling, J. Mater. Process. Technol. 209 (2009) 5167–5177.

[9] T. Özel, I. Llanos, J. Soriano, P.-J. Arrazola, 3D finite element modelling of chip formation process dfor machining Inconel 718: comparison of fe software predictions, Mach. Sci. Technol. 15 (2011) 21–46.

[10] T. Özel, D. Ulutan, Prediction of machining induced residual stresses in turning of titanium and nickel based alloys with experiments and finite element simulations, CIRP Ann. - Manuf. Technol. 61 (2012) 547–550.

[11] Y. Guo, D. Dornfeld, Finite element modeling of burr formation process in Drilling 304 stainless steel, J. Manuf. Sci. Eng. 122 (2002) 612–619.

[12] M. Abouridouane, F. Klocke, D. Lung, O. Adams, A new 3D multiphase FE model for micro cutting ferritic-pearlitic carbon steels, CIRP Ann. - Manuf. Technol. 61 (2012) 71–74.

[13] S.L. Soo, R.C. Dewes, D.K. Aspinwall, 3D FE modelling of high-speed ball nose end milling, Int. J. Adv. Manuf. Technol. 50 (2010) 871–882.

[14] G. Fang, P. Zeng, Three-dimensional thermo-elastic-plastic coupled FEM simulations for metal oblique cutting processes, J. Mater. Process. Technol. 168 (2005) 42–48.

[15] O. Pantalé, Modélisation et Simulation Tridimensionnelles de la Coupe des Métaux, (Ph.D. thesis), Université de Bordeaux I, 1996.

[16] O. Pantalé, R. Rakotomalala, M. Touratier, An ALE three-dimensional model of orthogonal and oblique metal cutting processes, Int. J. Form. Process. 1 (1998) 371–388.

[17] H. Kishawy, M. Elbestawi, Effects of process parameters on material side flow during hard turning, CIRP Ann. - Manuf. Technol. 39 (1999) 1017–1030.

[18] H. Kishawy, A. Haglund, M. Balazinski, Modelling of material side flow in hard turning, CIRP Ann. - Manuf. Technol. 55 (2006) 85–88.

[19] L. Illoul, P. Lorong, On some aspects of the CNEM implementation in 3D in order to simulate high speed machining or shearing, Comput. Struct. 89 (2011) 940–958.

[20] F. Ducobu, E. Rivière-Lorphèvre, E. Filippi, Application of the Coupled Eulerian-Lagrangian (CEL) method to the modeling of orthogonal cutting, Eur. J. Mech. - A/Solids 59 (2016) 58–66.

[21] F. Ducobu, E. Rivière-Lorphèvre, E. Filippi, Experimental contribution to the study of the Ti6Al4V chip formation in orthogonal cutting on a milling machine, Int. J. Mater. Form. 8 (2015) 455–468.

[22] SECO TOOLS, Turning catalog and technical guide 2012, SECO TOOLS AB, 2011.

[23] G. Johnson, W. Cook, A constitutive model and data for metals subjected to large strains, high strain rates and high temperatures, in: Proceedings of the Seventh International Symposium on Ballistics, The Hague, The Netherlands, 1983, pp. 541–547.

[24] F. Ducobu, E. Rivière-Lorphèvre, E. Filippi, On the importance of the choice of the parameters of the Johnson-Cook constitutive model and their influence on the results of a Ti6Al4V orthogonal cutting model, Int. J. Mech. Sci. 122 (2017) 143–155.

[25] S. Seo, O. Min, H. Yang, Constitutive equation for Ti-6Al-4V at high temperatures measured using the SHPB technique, Int. J. Impact Eng. 31 (2005) 735–754.

[26] J. Rech, P. Arrazola, C. Claudin, C. Courbon, F. Pusavec, J. Kopac, Characterisation of friction and heat partition coefficients at the tool-work material interface in cutting, CIRP Ann. - Manuf. Technol. 62 (2013) 79–82.

[27] T. Özel, E. Zeren, Numerical modelling of meso-scale finish machining with finite edge radius tools, Int. J. Mach. Mach. Mater. 2 (2007) 451–768.

[28] M. Nasr, E.-G. Ng, M. Elbestawi, Effects of workpiece thermal properties on machining-induced residual stresses - thermal softening and conductivity, Proceedings of the Institution of Mechanical Engineers, Part B: Journal of Engineering Manufacture, 221, 2007, pp. 1387–1400.

[29] P. Arrazola, T. Özel, Investigations on the effects of friction modeling in finite element simulation of machining, Int. J. Mech. Sci. 52 (2010) 31–42.

[30] F. Ducobu, P.-J. Arrazola, E. Rivière-Lorphèvre, E. Filippi, Finite element prediction of the tool wear influence in Ti6Al4V machining, Procedia CIRP 31 (2015) 124–129.